## Supplemental Material

# Control of bulk superconductivity in a BCS superconductor by surface charge doping via electrochemical gating

E. Piatti,[1] D. Daghero,[1] G. A. Ummarino,[1,2] F. Laviano,[1] J. R. Nair,[1]
R. Cristiano,[3] A. Casaburi,[4] C. Portesi,[5] A. Sola,[5] and R. S. Gonnelli[1]

[1]*Department of Applied Science and Technology, Politecnico di Torino, Torino, Italy*
[2]*National Research Nuclear University MEPhI, Moscow Engineering Physics Institute, Moskva, Russia*
[3]*CNR-SPIN Institute of Superconductors, Innovative Materials and Devices, UOS-Napoli, Napoli, Italy*
[4]*School of Engineering, University of Glasgow, Glasgow, UK*
[5]*INRIM - Istituto Nazionale di Ricerca Metrologica, Torino, Italy*

### I. COMPOSITION OF THE PES

We employed two different PES compositions in different sets of experiments, in order to rule out any influence of the specific electrolyte formulation on the measured effects: i) a Li-TFSI based PES we have already used in the experiments on noble metals[S1,S2]; ii) a similar PES where the Li-TFSI-PEGMA mixture was substituted by pure 1-Butyl-1-methylpiperidinium bis(trifluoromethylsulfonyl)imide ionic liquid.

### II. ION MILLING

All the measurements described in the present paper were made on two different NbN devices, whose thickness was progressively reduced by Ar-ion milling. In other words, once the FE measurements for a given thickness were completed, we removed the PES by rinsing the device in ethanol, then carefully cleaned the surface via sonication in acetone and ethanol. The physical removal of NbN was then performed by an Electron Cyclotron Resonance Plasma System operating at 2.45 GHz, in which the sample was placed 10 cm above the plasma source. The milling was carried out at an Ar pressure of $1.0 \times 10^{-3}$ mbar and, using an extraction voltage of 400 V and an anode current density of 1.5 mA cm$^{-2}$, an etching rate of 0.14 nm s$^{-1}$ was obtained. The whole sample area was exposed to the ion flux; since the ions etch the MgO substrate more efficiently than the NbN film, the milling process was calibrated on an unpatterned film with the help of a profilometer (by measuring the height difference between the exposed area and a region protected by a polymeric mask). The exposure time was optimized to allow for a thickness reduction of about 10 nm in each milling step. After each milling step, we characterized the surface morphology of the device via AFM. This was to ensure that the quality of the surface did not get degraded in a significant way.

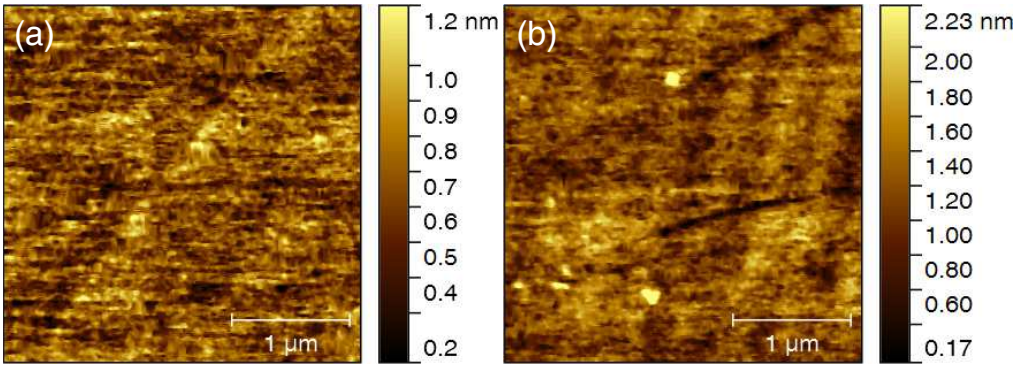


FIG. S1: AFM topography maps of the active channel of the same NbN device. Panel (a) shows the surface of the pristine film. Panel (b) shows the surface of the film after three ion milling steps. Both maps are 3 $\mu$m $\times$ 3 $\mu$m in lateral dimension. Scale bars on the left show the AFM heigth signal for the two maps.

Figure S1 shows two 3 $\mu$m $\times$ 3 $\mu$m topography maps of the same device. The map on the left was measured on the pristine device, before any ion milling steps ($t = 39.2 \pm 0.8$ nm). The map on the right was measured after three ion milling steps, i.e. for the smallest film thickness reached in our experiments ($t = 9.5 \pm 1.8$ nm). The pristine sample appears to be almost atomically flat, with a terrace clearly visible across the map. The milled sample presents a somewhat rougher surface, as is to be expected. Both maps feature a surface roughness below 1 nm. In order to obtain a reliable estimation of the roughness of our devices, we measured several topography maps in different regions of the devices and calculated the arithmetic average of the 2D roughness profile ($R_a$) for each map. We then averaged the $R_a$ themselves for each milling step. By this method, the pristine devices showed $R_a = 0.32 \pm 0.06$ nm. After the first ion milling step, the surface roughness increased to $R_a = 0.45 \pm 0.15$ nm. The second and third ion milling steps did not degrade the surface further.

## III. DETAILS OF TRANSPORT MEASUREMENTS

Transport measurements were performed in a Cryomech® ST-403 3K pulse-tube cryocooler. The source-drain current $I_{SD}$ was provided by a Keithley 6221 source and was kept sufficiently small (a few tens of $\mu$A) so as to avoid heating in the film (even in the thinnest ones). The possible thermoelectric effects were eliminated by inverting the current within each measurement[S1]. The longitudinal voltage drops along the active and reference channels, $V^{active}$ and $V^{ref}$, were measured by a low-noise Keithley 2182A nanovoltmeter, and the sheet resistance $R_\square$ of each channel was calculated accordingly. The measurements were performed during both cool-down to 2.7 K and subsequent warm-up to room temperature. However, since the mobility of the ions in the PES is strongly damped below the glassy transition of the PES, every change in $V_G$ had to be performed at high temperature (above 230 K) and the only way to detect a $T_c$ shift was to compare resistance curves obtained in different thermal cycles. To maximize the reproducibility of the $T_c$ measurement, we only considered the heating curves for the analysis, since the warming up was quasistatic. Nevertheless, the variation in $T_c$ measured in the same channel in different heating processes was comparable to the shift due to EDL gating. It is precisely to overcome this problem that we measured at the same time the resistance of the active (gated) and of the reference (ungated) channels. Figure S2 presents a sketch of the full device, showing both the region of the film that is capacitively coupled to the gate electrode (active channel) and the region that is not (reference channel).

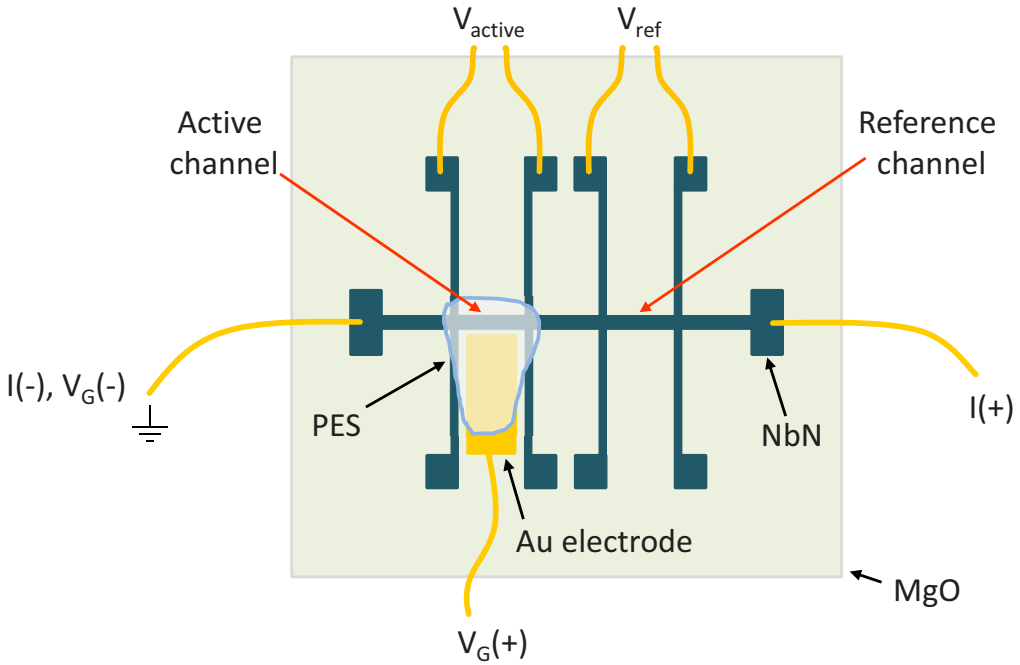


FIG. S2: Sketch of a gated NbN device. The edges of the PES, that define the area of the device capacitively coupled to the gate electrode, are highlighted in blue for clarity.

A further possible source of systematic error in the measurements lies in the fact that, in general, the modulation to the carrier density induced by EDL gating may be slightly temperature-dependent[S3,S4]. Thus, the measurement

of the induced charge performed at room temperature by Double-Step Chronocoulometry may not correctly estimate the carrier density modulation affecting the superconducting properties at low temperature. While this is a known issue in EDL-gated 2D materials and may be due to disorder[S3] or charge-ordering[S4], we don't expect it to play a significant role in metallic thin films. Indeed, if the density of extra charge carriers introduced by the gate was temperature-dependent, we would expect the resistance modulation in the normal state to be temperature-dependent as well. Instead, our earlier results on gold[S1] and other noble metals[S2] showed that the $R$ vs. $T$ curves are rigidly shifted by the applied gate voltage, with no sign of a further temperature-dependent component. We can thus discard the possibility of a significant temperature dependence of the induced carrier density in our metallic films.

## IV. REVERSIBILITY OF THE $T_c$ SHIFT

In order to check the purely electrostatic nature of the $T_c$ modulation, i.e. to ensure that the $T_c$ shift was completely reversible upon removal of the gate voltage, we performed measurements of $R_\square(T)$ at zero gate voltage before and after the application of each $V_G$. This was necessary due to the ubiquitous possibility that electrochemical reactions occur at the electrolyte/electrode interface, leading to permanent or semipermanent modifications of the material under study[S5]. Figure S3 shows five $R_\square(T)$ curves measured subsequently in the 18.3 nm thick device, with $V_G$ = 0, +3 V, 0, -3 V, 0. Note that the horizontal scale is the absolute temperature (i.e. not the referenced one). The three curves recorded at $V_G = 0$ fall exactly on top of each other, the very small shift being only due to the different heating runs and thus being completely corrected if the referenced temperature is used. The longest consecutive series of measurements where the reproducibility of the $V_G = 0$ curve was checked featured seven different $V_G$ values, for a total of 15 thermal cycles. This reproducibility confirms the absence of significant electrochemical interaction between the PES and the NbN thin film even when a gate voltage of ±3 V is applied.

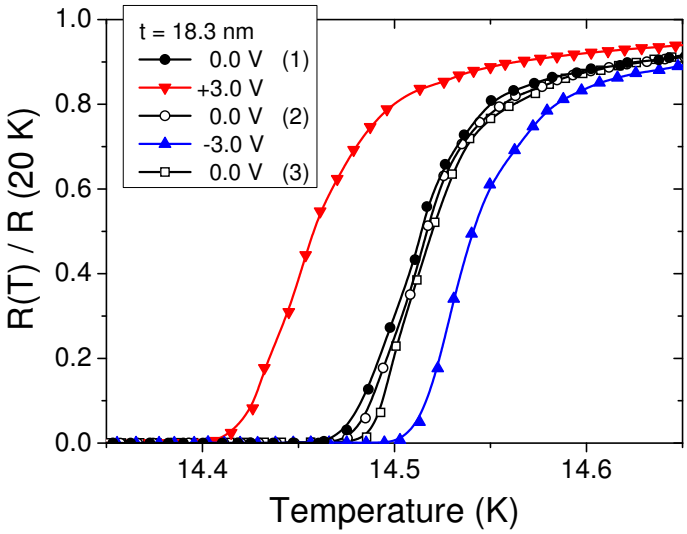


FIG. S3: Five $R_\square(T)$ curves measured subsequently in the 18.3 nm thick device. The superconducting transition temperature at $V_G = 0$ returns to the original value after applying and removing a gate voltage $V_G = +3$ V and $V_G = -3$ V, confirming the complete reversibility of the effect and thus its purely electrostatic origin.

The 9.5 nm thick device was anomalous in this sense. In that case, the superconducting transition temperature did not go back to the original value upon removal of the gate voltage. Instead, we observed a positive irreversible $T_c$ shift in addition to the usual (reversible) electrostatic effect, independently of the sign of the gate voltage. Remarkably, the transition profiles remained unaffected. By using the technique described above and shown in Fig.S3, we were able to separate the irreversible effect from the reversible one. The $T_c$ shifts shown in Fig. 2 and 3 of the main text are only the *reversible* ones; conservatively, we only reported the data for which the reversible effect was much greater than the irreversible one. While a quantitative explanation for this slow relaxation in the $T_c$ of NbN at small film thicknesses is beyond the scope of this paper, we can provide a qualitative assessment of the problem. It is very well known that the NbN and MgO unit cells feature a mismatch of $\sim 3\%$[S6]. This can result in a native strain in NbN films grown on MgO for film thicknesses below $\sim 50$ nm[S6]. This mismatch can also lead to the formation of slightly misaligned three-dimensional islands during the growth process, with structural defects such as dislocations, vacancies and voids in films up to $\sim 15$ nm thick[S6]. By ion-milling our films, we eventually expect to directly expose this damaged and

strained region to the PES and the intense electric field built up in the EDL. We thus interpret the progressive shift in $T_c$ upon several thermal cycles under the presence of the electric field as a parasitic electrostriction effect that induces a progressive relaxation of the strained NbN in close proximity to the mismatched MgO substrate. This effect is thus completely negligible for films of larger thickness, that would be significantly less defective and feature a lower strain, as also demonstrated by the reversibility of the $T_c$ shifts that we indeed measured in these thicker films. For the same reason, we decided not to apply the model for the proximity effect to the values of $\Delta T_c$ measured in the 9.5-nm thick device (see Figure 4 of the main text). Since the irreversible $T_c$ shift was likely to become worse at even smaller thicknesses, we opted not to thin down our devices further. Another reason why we did not explore thicknesses below 9.5 nm is that we were not confident that the film would retain a sufficient electrical continuity and a proper surface quality upon further ion-milling steps.

## V. DENSITY FUNCTIONAL THEORY CALCULATIONS OF THE NbN DENSITY OF STATES

The total density of states (DOS) of the bulk crystalline NbN has been ab-initio calculated by density functional theory (DFT) employing the all-electron full-potential linearised augmented-plane-wave (FP-LAPW) method as implemented in the Elk code[S7]. In order to describe the exchange and correlation energy term we adopted the Generalised Gradient Approximation (GGA) as developed in Ref. S8. The Brillouin zone was sampled with a $24 \times 24 \times 24$ mesh of $k$-points and the convergence of self-consistent field calculations was attained with a Kohn-Sham effective potential tolerance of $1{\times}10^{-9}$ and a total energy tolerance of $1{\times}10^{-8}$ Hartree. The DOS close to the Fermi energy ($E_F$) has been calculated with an energy resolution of 3 meV between -0.6 and +0.6 eV from $E_F$. The electronic band structure in the $k$-space and the total DOS (calculated in the range from -13.6 eV to 13.6 eV with respect to $E_F$ and with an energy resolution of 5 meV) are in very good agreement with the results in the literature[S9,S10].

## VI. FURTHER DETAILS ABOUT THE PROXIMITY-EFFECT MODEL

As explained in the text, we used a strong-coupling model for the proximity effect[S11] to calculate the relationship between the experimental critical temperature of the film, treated as a compound slab, and the surface density of induced charges $\Delta n_{2D}$. To do so, we assumed the induced carrier density per unit volume in the surface layer (i.e. $\Delta n_{3D}(z)$) to follow a step-like profile as a function of the depth $z$. We called $d_s$ the thickness of the charge-induction layer. According to that model, for a given value of $\Delta n_{2D}$ and $d_s$, the computed $T_{c,comp}$ of the compound slab varies with the total film thickness $t$ in a way that qualitatively agrees with the experimental trend at low and moderate induced carrier densities: The difference between $T_{c,comp}$ and the unperturbed critical temperature is strongly reduced by increasing $t$, eventually becoming comparable with the experimental uncertainty for $t > 100$ nm.

In Fig. S4 the experimental values of the $T_c$ shift are reported as a function of the film thickness $t$ for three different values of $\Delta n_{2D}$, i.e. $1 \times 10^{14}\,\mathrm{cm}^{-2}$ (black symbols), $7 \times 10^{14}\,\mathrm{cm}^{-2}$ (red symbols) and $12 \times 10^{14}\,\mathrm{cm}^{-2}$ (blue symbols). In the first two cases (black and red solid lines), the experimental data can be reproduced fairly well by using the same value of $d_s = 4.4$ Å ([1]) – which, by the way, corresponds to the height of the unit cell. In this range of $\Delta n_{2D}$, the induced volume charge density $\Delta n_{3D}$ in the surface layer results in a displacement of the Fermi level that corresponds to a reduction in the DOS (see Fig. 4a in the main text). At the highest value of $\Delta n_{2D}$, however, the same $d_s$ would lead to such a high value of $\Delta n_{3D}$ that the Fermi level would be pushed well beyond the local minimum, leading to an *increase* in the DOS, and a consequent *increase* in the $T_c$, contrary to the experimental finding. The blue solid line in Fig.S4 represents the $\Delta T_c$ vs. $t$ calculated in this case.

To obtain an agreement with the experimental data for $\Delta n_{2D} = 12 \times 10^{14}\,\mathrm{cm}^{-2}$, the value of $d_s$ must be increased to 6.6 Å (dashed blue line). It is also worthwhile to note that, according to the model, if the change in the critical temperature of the surface layer, $T_{c,s}$, was larger than a few Kelvin, the resulting $T_{c,comp}$ would be comparable with $T_{c,s}$; in other words, for large modifications of $T_{c,s}$ the proximity effect would play almost no role in determining the final $T_{c,comp}$. This result is in agreement with recent findings on EDL-gated FeSe thin flakes[S12,S13].

---

[1] This value of $d_s$ is just a guess. For $\Delta n_{2D} = 1 \times 10^{14}\,\mathrm{cm}^{-2}$ it differs from that reported in Figure 4 of the main text, which was instead determined by the iterative best-fit procedure described there.

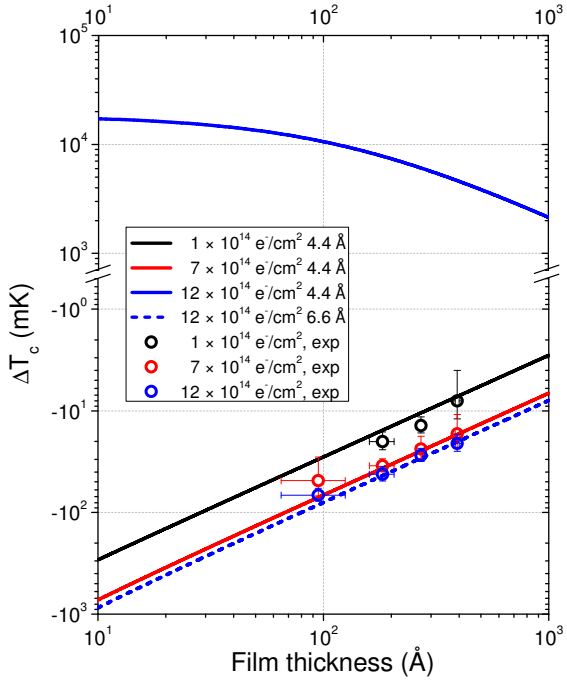


FIG. S4: Critical temperature shift, $\Delta T_c$, vs. film thickness for three selected values of accumulated electron density ($\Delta n_{2D}$ = 1, 7, $12 \times 10^{14}\,\mathrm{cm}^{-2}$). Solid (dashed) lines result from the proximity effect model for a surface layer thickness of 4.4 Å (6.6 Å).

## VII. VALIDITY OF THE COOPER LIMIT APPROXIMATION

Eq. 2 of the main text is rigorously valid as long as the superconducting order parameter can be assumed to be uniform within each layer (Cooper limit). This, in turn, requires each layer $(s, b)$ to be thinner than the corresponding Gor'kov coherence length $\xi_{\mathrm{G}}|_{\mathrm{s,b}}$[S14,S15]. This length is $\xi_{\mathrm{T}} = \hbar v_{\mathrm{F}}/2\pi k_B T$ in the clean limit or $(\frac{1}{3}\xi_{\mathrm{T}} l)^{\frac{1}{2}}$ in the dirty limit, where $l$ is the electron mean free path[S15]. In general, the Gor'kov coherence length is different in the normal and superconducting sides of the junction due to the different Fermi velocities and mean free paths in the two materials. In our case, however, the material is the same and thus these two quantities coincide. We estimate $l \simeq 1$ nm for our films from Hall effect and sheet resistance measurements; combining these with $v_{\mathrm{F}} \simeq 2 \cdot 10^6$ m/s from Ref. S16 gives a Gor'kov coherence length $\xi_{\mathrm{G}} \simeq 10$ nm at $T \sim T_c$. This indicates that the thin surface layer perturbed by the electric field is always within the Cooper limit; the situation for the underlying bulk is however more complex, as Fominov and Feigel'man showed[S17] that a high transparency of the tunneling barrier between the two layers can lead to an enhancement in the coherence length ([2]).

Nevertheless, the agreement between the theoretical model in the Cooper limit and the experimental results is striking, suggesting that the model is applicable even if its limits of validity are not strictly met. Indeed, in the same article where he developed the strong-coupling proximity effect model[S11], Silvert also indicates an empirical test to assess the validity of the Cooper limit in films where the condition $d_{s,b} \ll \xi_{\mathrm{G}}$ could not be ascertained. This test requires $\Delta T_c$ to depend only on the ratio $d_b/d_s$. As we show in Fig. S5, the $T_c$ shift scales with $d_b/d_s$ for a wide range of values of $\Delta n_{2\mathrm{D}}$, irrespectively of the specific values of $d_s$ and $d_b$. We thus conclude that the model of Ref. S11 is applicable to our films even if the Cooper limit is only marginally satisfied for the bulk layer of our "compound slab".

We also note that in general the correct averaging of the electron-phonon coupling constants between the normal and superconducting layers (Eq. 2 of the main text) is also dependent on the transparency of the barrier[S17]. If the conductivity is large but finite, the result from Ref. S11 holds. If the interface is perfectly transparent (infinite barrier

[2] An ideal total transparency of the tunneling barrier is also commonly referred to as the Cooper limit. We stress that, in this discussion, we always intend the Cooper limit as constancy of the order parameter and not as infinite barrier conductivity.

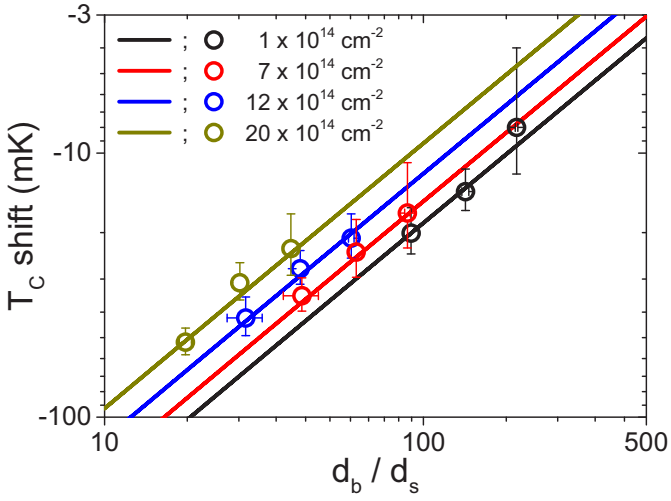


FIG. S5: Scaling of the critical temperature shift, $\Delta T_c$, vs. the ratio $d_b/d_s$ for four different values of accumulated electron density ($\Delta n_{2D} = 1,\ 7,\ 12,\ 20 \times 10^{14}\,\mathrm{cm}^{-2}$). Solid lines result from the proximity effect model in the Cooper limit.

conductivity), the average is weighted on the layer thicknesses only[S17]. Since in our case the exact value of the barrier conductivity is unknown, we also performed calculations assuming total transparency. These results are within $\sim 20\%$ of the finite barrier conductivity model, a difference which is smaller than the other sources of uncertainty in our calculations (mainly, the estimation of $\Delta n_{2D}$ from Double-Step Chronocoulometry).

Finally, we stress that the second main result of this work (i.e., the existence of an upper limit for the modulation of the volume carrier density at the surface) does not rely on the Cooper limit to be satisfied, as it depends only on the shape of the DOS at larger electron filling. This is because we do not observe any positive $T_c$ shift for $V_G > 0$, which mandates that the Fermi level has not been shifted too far beyond the local minimum in the DOS even for the largest values of $\Delta n_{2D}$. This *qualitative* behavior is thus independent on the details of the proximity effect model. The validity of the Cooper limit, which we have here discussed, is instead required for a *reliable, quantitative* assessment of the value of this upper limit beyond an order-of-magnitude estimation.

## VIII. ELECTROSTATIC SCREENING BEYOND THE LINEAR REGIME FOR A PLANAR DISTRIBUTION OF CHARGES IN A METAL

In order to try to explain the anomalous screening length determined at very high induced charge density by the proximity-effect model we applied the screening theory beyond the linear regime[S18]. In this case the standard approximation at the basis of the linear regime in a metal, i.e. $|e\phi| \ll E_F$ (where $\phi$ is the electrostatic potential of the induced charge and $E_F$ is the Fermi energy of the metal), doesn't hold any more. For a planar distribution of charges in a degenerate Fermi gas this theory predicts a general equation that involves the integral of the density of states $N(E)$ of the metal (see Ref. S18, pag. 46, eq. II-7):

$$\pm\sqrt{\frac{2}{\epsilon_r\epsilon_0}}z = \int_{\phi_S}^{\phi} \frac{d\varphi}{\left(\int_0^{\varphi} -e d\varphi' \int_{E_F+e\varphi'}^{E_F} N(E)dE\right)^{1/2}} \tag{S1}$$

where $\epsilon_r$ is the relative permittivity, $z$ is the coordinate perpendicular to the planar charge distribution, directed toward its inner part, and $\phi_S$ is the potential at its surface, i.e. $\phi_S = \phi(z=0)$. We know the behaviour of $N(E)$ close to $E_F$ from ab-initio DFT calculations. Thus by inserting in eq. S1 a linear approximation for $N(E)$ in the electron accumulation region (see fig. 2a of Ref. S5), $N(E) = N(E_F) - k(E - E_F)$, we can integrate equation S1 obtaining:

$$\phi(z \geq 0) = \frac{a}{b}\left\{1 - \tanh^2\left[\frac{\sqrt{a}}{2}\sqrt{\frac{2}{\epsilon_r\epsilon_0}}z + \tanh^{-1}\left(\frac{\sqrt{a - b\phi_S}}{\sqrt{a}}\right)\right]\right\}. \tag{S2}$$

Here $a = e^2N(E_F)/2$ and $b = e^3k/6$ are known from DFT calculations (see also[S19] for comparison). As a consequence the $z$ dependence of the potential $\phi(z)$ is fully determined by the choice of the surface potential $\phi_S$. This choice is not arbitrary since we can select the $\phi_S$ value in order to match the experimental induced surface charge density $\Delta n_{2D}$ that is given by:

$$\Delta n_{2D} = \int_0^\infty \frac{\epsilon_r \epsilon_0}{e} \frac{d^2\phi(z)}{dz^2} dz. \tag{S3}$$

In the framework of this theory beyond the linear regime we calculate the screening length as the $z$ coordinate at which the volume charge density $\Delta n_{3D} = (\epsilon_r\epsilon_0/e)\left(d^2\phi\left(z\right)/dz^2\right)$ is $1/e$ of its surface value $\Delta n_{3D}(z=0)$. When $\Delta n_{2D} \lesssim 1 \times 10^{14}\text{cm}^{-2}$ this length coincides (within 10 %) with the screening length given by the standard Thomas-Fermi theory $\lambda_{TF} = \sqrt{\epsilon_r\epsilon_0/2a} \simeq 0.2$ nm and nicely corresponds to the constant value determined from the experiments (see Fig. 4b of the main text). At the increase of $\Delta n_{2D}$ the screening length in the non-linear regime progressively increases reaching 0.36 nm when $\Delta n_{2D} = 5.35 \times 10^{14}\text{cm}^{-2}$, again in very good agreement with the experimental results shown in Fig. 4b. For larger values of $\Delta n_{2D}$ this theory is no more able to explain the observed linear increase of the screening length that thus remains an open problem.


[S1] D. Daghero, F. Paolucci, A. Sola, M. Tortello, G. A. Ummarino, M. Agosto, R. S. Gonnelli, J. R. Nair, and C. Gerbaldi, *Phys Rev. Lett.* **108**, 066807 (2012)

[S2] M. Tortello, A. Sola, K. Sharda, F. Paolucci, J. R. Nair, C. Gerbaldi, D. Daghero, and R. S. Gonnelli, *Appl. Surf. Sci.* **269**, 17 (2013)

[S3] J. T. Ye, S. Inoue, K. Kobayashi, Y. Kasahara, H. T. Yuan, H. Shimotani, and Y. Iwasa, *Nature Materials* **9**, 125 (2010)

[S4] L. J. Li, E. C. T. O'Farrell, K. P. Loh, G. Eda, B. Özyilmaz, and A. H. Castro Neto, *Nature* **529**, 185 (2016)

[S5] E. Piatti, A. Sola, D. Daghero, G. A. Ummarino, F. Laviano, J. R. Nair, C. Gerbaldi, R. Cristiano, A. Casaburi, and R. S. Gonnelli, *J. Supercond. Nov. Magn.* **29**, 587591 (2016)

[S6] L. Hultman, L. R. Wallenberg, M. Shinn, and S. A. Barnett, *J. Vac. Sci. Technol. A* **10**, 1618 (1992)

[S7] The Elk FP-LAPW Code. http://elk.sourceforge.net/

[S8] Y. Zhang and W. Yang, *Phys. Rev. Lett.* **80**, 890 (1998)

[S9] AFLOW Automatic-FLOW for material discovery, Center for Material Genomics, Material Science, Duke University, 2016. http://www.aflowlib.org/

[S10] T. Amriou, B. Bouhafs, H. Aourag, B. Khelifa, S. Bresson, and C. Mathieu, *Physica B* **325** 46 (2003)

[S11] W. Silvert, *Phys. Rev. B* **12**, 4870 (1975)

[S12] J. Shiogai, Y. Ito, T. Mitsuhashi, T. Nojima, and A. Tsukazaki, *Nature Phys.* **12**, 42 (2016)

[S13] B. Lei, J. H. Cui, Z. J. Xiang, C. Shang, N. Z. Wang, G. J. Ye, X. G. Luo, T. Wu, Z. Sun, and X. H. Chen, *Phys. Rev. Lett.* **116**, 077002 (2016)

[S14] P. G. de Gennes, *Rev. Mod. Phys.* **36**, 225 (1964)

[S15] J. R. Waldram, *Superconductivity of Metals and Cuprates*, Chapter 11: Further theory and properties, Section 11.1: The proximity effect, IOP Publishing Ltd, Bristol and Philadelphia (1996)

[S16] S. P. Chockalingam, M. Chand, J. Jesudasan, V. Tripathi, and P. Raychaudhuri, *Phys. Rev. B* **77**, 214503 (2008)

[S17] Ya. V. Fominov and M. V. Feigel'man, *Phys. Rev. B* **63**, 094518 (2001)

[S18] J.-N. Chazalviel, *Coulomb screening by mobile charges: applications to materials science, chemistry, and biology*, Chapter II: Screening of a Static Charge Distribution Beyond the Linear Regime, Springer Science+Business Media, New York (1999)

[S19] S. Blackburn, M. Côté, S. G. Louie and M. L. Cohen, *Phys. Rev. B* **84**, 104506 (2011)